Journal Pre-proof

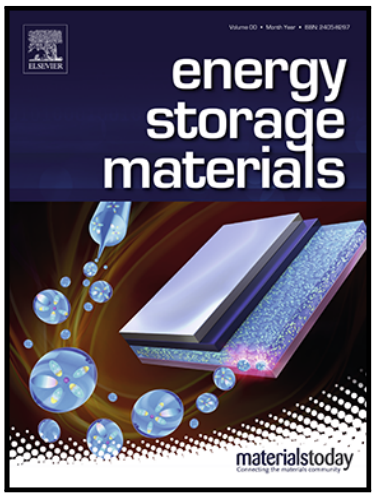

Assessing the Critical Current Density of All-Solid-State Li Metal Symmetric and Full Cells

So-Yeon Ham , Hedi Yang , Omar Nunez-cuacuas , Darren H.S. Tan , Yu-Ting Chen , Grayson Deysher , Ashley Cronk , Phillip Ridley , Jean-Marie Doux , Erik A. Wu , Jihyun Jang , Ying Shirley Meng

PII: S2405-8297(22)00670-5
DOI: https://doi.org/10.1016/j.ensm.2022.12.013
Reference: ENSM 2595

To appear in: *Energy Storage Materials*

Received date: 21 July 2022
Revised date: 20 November 2022
Accepted date: 9 December 2022

Please cite this article as: So-Yeon Ham , Hedi Yang , Omar Nunez-cuacuas , Darren H.S. Tan , Yu-Ting Chen , Grayson Deysher , Ashley Cronk , Phillip Ridley , Jean-Marie Doux , Erik A. Wu , Jihyun Jang , Ying Shirley Meng , Assessing the Critical Current Density of All-Solid-State Li Metal Symmetric and Full Cells, *Energy Storage Materials* (2022), doi: https://doi.org/10.1016/j.ensm.2022.12.013

Assessing the Critical Current Density of All-Solid-State Li Metal Symmetric and Full Cells

So-Yeon Ham[a], Hedi Yang[b], Omar Nunez-cuacuas[b], Darren H. S. Tan[b], Yu-Ting Chen[a], Grayson Deysher[a], Ashley Cronk[a], Phillip Ridley[b], Jean-Marie Doux[b], Erik A. Wu[b], Jihyun Jang[b,*], and Ying Shirley Meng[b,c,*]

[a] Materials Science and Engineering Program, University of California San Diego, La Jolla, 92093, United States.

[b] Department of NanoEngineering, University of California San Diego, La Jolla, California 92093, United States.

[c] Pritzker School of Molecular Engineering, University of Chicago, Chicago, Illinois 60637, United States.

Corresponding Authors

* Jihun Jang: jijang@ucsd.edu, * Ying Shirley Meng: shirleymeng@uchicago.edu

Highlights

- Critical current density of all-solid-state Li metal batteries were evaluated and compared in symmetric and full cell.
- The relationship between fabrication pressure applied duration and critical current density in symmetric cell were revealed.
- A constant pressure setup mitigates the volume change during cycling, and effectively increase the critical current density of the full cell.

Graphical Abstract

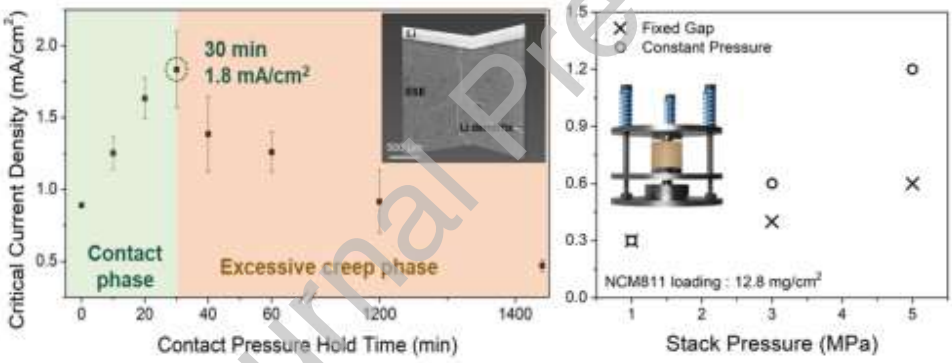

Abstract

All-solid-state Li metal batteries (Li-ASSBs) have drawn much attention in recent years owing to their potential in achieving high energy densities. However, the low critical current density (CCD) of Li-ASSBs at room temperature remains a major bottleneck which limits the prospects for commercialization. Most studies reported so far have demonstrated CCDs significantly lower than conventional lithium-ion batteries, along with a lack of consistency across such reports. While these CCD inconsistencies can be attributed to variations in pressure, temperature, and

solid electrolyte chemistry, crucial parameters often omitted in the literature, such as the fabrication pressure used and duration for which it is applied, both of which are required to achieve good contact between Li metal and the solid electrolyte. Here, the relationship between the fabrication pressure contact hold time of Li metal versus CCD is reported, thus elucidating the effect of controlled Li deformation on the CCD. The CCDs for symmetric and full cell architectures are also evaluated, where the effect of volumetric expansion and associated changes in cell stack pressure are examined. Finally, a constant pressure cell design is introduced to mitigate the negative effects of volume change during cycling, allowing the Li-ASSB to achieve higher CCDs at room temperature.

Keywords

All-solid-state battery, critical current density, Li metal anode, volume expansion, stack pressure

1. Introduction

Lithium metal batteries, with their promise of high energy density, have gained much attention in recent years due to the high energy densities achieved through the use of Li metal anodes with high theoretical capacity (3860 mAh/g) and the lowest electrochemical potential (−3.04 V vs Standard Hydrogen Electrode) [1]. However, it still presents a myriad of challenges including poor Coulombic efficiency from continued irreversible reaction with liquid organic electrolyte and Li dendritic growth resulting in an abnormal safety issue [2]. All-solid-state Li metal batteries (Li-ASSBs) have recently emerged with the intrinsic advantages of the absence of organic materials which can react as resources of combustion and inhibition subsequent electrolyte decomposition [3]. However, Li-ASSBs are also often limited by low critical current

densities (CCDs). The CCD can be defined as the certain current density (mA/cm^2) at which a cell failure occurs when the growth of Li dendrite from the Li metal anode reaches the cathode side through the solid-state electrolyte (SSE) separator making a short circuit between cathode and anode, which results in vigorous self-discharge and thus safety issue in a real cell [2,3]. Extensive research on Li-ASSBs has resulted in architectures that can achieve 1000 cycles at 3.4 mA/cm^2 at 60°C by enabling dendrite-free Li metal anode [4]. Although high CCDs are obtained at elevated temperatures which is comparable with conventional lithium metal batteries having liquid electrolytes, achieving improved room temperature performance needs further investigation. Interestingly, the CCDs of Li-ASSBs reported in the literature vary widely, as summarized in Figure S1. While CCD is dependent on the cell chemistry, cell stack pressure, and plating capacity, there are still large CCD variations reported even for similar cell configurations [5,6], and showed the wide range of CCDs even in our work in which the same configuration was used (the variable here will be discussed later). This indicates that there are vital parameters during cell fabrication which have not yet been considered or compared in the previous literature. Nonetheless, general trends can be observed throughout all the Li-ASSB CCDs reported. First, it is clear that cells under elevated temperature operation exhibit higher CCDs compared to those at room temperature. This is widely attributed to the improved diffusion kinetics and favorable mechanical properties that promote uniform Li metal plating [7,8]. However, if the room or near-room temperature remains to be the favorable operating condition for practical Li-ASSBs, greater focus should be placed on increasing the CCD without the use of elevated temperatures.

When comparing cell architectures, studies using only symmetric cells [8–22] often report higher CCDs compared to full cells [4,16,23–25] at a similar cycling temperature. While the reason for this disparity is not yet understood, it is clear that high CCD values reported in the

literature using symmetric cell configurations cannot be reproduced in full cell formats at room temperature [26, 27, 28]. As a result, some full cell performance reports adopt elevated temperature (>55°C) to demonstrate cyclability, citing the need to overcome slow diffusion kinetics at the cathode-solid electrolyte interface [29]. However, this explanation is inconsistent with studies reporting high current densities (>5.0 mA/cm^2) operations at room temperature using similar composite cathode and alloy-based anodes such as lithium-indium or silicon anodes [30]. One plausible explanation was rationalized through the misinterpretation of the cell shorting voltage features. Yang *et al*. described this as the "fake stable" phenomena, where symmetric cell polarization curves are easy to be misinterpreted as stable when in fact a short circuit has already occurred [31]. In such scenarios, a typical flat voltage curve is still observed even when cycled at high current densities (>10 mA/cm^2), where polarization originated from the ohmic resistance of the electron pathway within the shorted circuit. This misunderstanding cannot occur in a full cell where the cell voltage is determined by the state-of-charge of the cathode electrode, thus any occurrence of a short circuit would manifest as an obvious voltage fluctuation from the typical cathode charge curve. Lewis *et al.* also proposed the need to consider the areal capacity difference used in symmetric cell versus full cell tests, where the cell short phenomenon was found to only occur when an areal capacity of > 3 mAh/cm^2 for lithium plating and stripping was used [32]. This value is far more than most areal capacities used in symmetric cell tests, which typically use long hours of plating and stripping with < 1 mAh/cm^2 areal capacity [27]. There have been studies to mitigate the cell shorting by improving Li metal and SSE interface. Su *et al.* demonstrated that using graphite on the Li side would prevent chemical reaction between SSE and Li and also serve as mechanical constriction to enable high pressure cycling [28]. Another approach was to form more stable SEI by introducing polymer

electrolyte initiator [33] and adding Li_xSiO_x-enriched layer [34]. Li metal dentrite could form within a solid electrolyte layer if the electronic conductivity is not low enough. Han *et al.* studied Li deposition within the various SSE layers [35]. The group demonstrated that Li dendritic growth within the electrolyte layer was not significant at room temperature due to the low electronic conductivity. The electrolytes used in the research were $Li_7La_3Zr_2O_{12}$ (LLZO) and Li_3PS_4, having the electronic conductivity of 5.8×10^{-8} to 10^{-7} S/cm. In addition, stack pressure is one of the most important factors that dictate a CCD of Li-ASSB. Previous studies have found that relatively small changes in stack pressures can greatly affect the CCD, where it was reported that the CCD improves with increasing stack pressure, within a pressure range of 0.4 – 7 MPa [36][37]. However, the stack pressure on a Li-ASSB cannot be exceedingly high because that can induce both mechanical short due to Li deformation along with separator layer or an electrochemical short-circuit during Li metal plating, as shown in our previous work [38]. Yan *et al.* also showed the adjustment of stack pressure could resolve void formation by the Li deformation due to the low modulus characteristic of Li metal [39]. Interestingly, the symmetric cell shows much less volume change during cycling since the volumetric expansion arising from Li plating is compensated at the counter electrode which undergoes stripping simultaneously. However, this is not the case in full cell configurations, where a large amount of volumetric expansion due to Li plating cannot be compensated for the cathode side during de-intercalation. Thus, dynamic stack pressure effects on CCD during cycling must be investigated, but most studies only have adopted fixed gap cell setups where cell stack pressure is defined before cell operation. Given the stack pressure effects on CCD, it is reasonable to think that variable stack pressures in full cells can result in vast disparities in CCD findings compared to symmetric cells.

In this work, we discuss the stack pressure factors governing CCDs of both Li metal symmetric and full cells using common Li-ASSB cell configurations, Li | Li_6PS_5Cl (LPSCl) | Li symmetric cell and NCM811 | LPSCl | Li full cell. We demonstrate that, among the fabrication and operation parameters, the contact time between Li and SSE while fabrication can be also the critical factor which can dramatically affect the CCD values in symmetric cells. In addition, we also systemically addressed the root cause of CCD disparities between symmetric and full cells through the *operando* pressure monitoring while cell preparation and cycling. Finally, we reveal that the use of a constant pressure cell design can release pressure variation-driven stresses inside the cell while cycling which helps to achieve a higher CCD in Li-ASSBs operating near room temperature.

2. Material and methods

2.1. Materials preparation

Li_6PS_5Cl (LPSCl, NEI Corporation, USA) was used for solid-state electrolyte (SSE) separator layer and cathode composite preparation. For cathode composite purpose, the LPSCl particle size was reduced using E_{MAX} ball mill (Retsch, Germany). The ball milling was conducted for 2 hours at 300 rpm, using anhydrous xylene as a medium. Vapor grown carbon fiber (VGCF) was purchased from Sigma Aldrich (Graphitized, Iron-free), and dried overnight at 160°C under vacuum to remove moisture. NCM811 (LG Chem, Republic of Korea), coated with a boron-based layer, was used as received. Cathode composite was prepared by hand-mixing using a weight ratio of NCM811: LPSCl : VGCF = 66 : 31 : 3. Li metal (FMC, USA) foil was cleaned by scratching of the oxide layer and subsequently punched into 0.785 cm^2 area.

2.2. Materials characterization

Versa 510 (Zeiss/Xradia) X-ray microscope was used to investigate computed tomography (CT) of Li metal symmetric cell, with an objective of 20X, a source voltage of 80 kV and a power of 6.5 W, using the LE2 filter. The 360-degree scan was conducted in 15 sec exposure setting, for 2401 projections. The reconstruction of data was performed with Amira 2019.1 (ThermoFisher Scientific). After the reconstruction, the 3D view of inside was shown using box cutting function of Amira 2019.1 software. The solid-state cell was built in custom-made 2 mm internal diameter drilled PTFE rod. The reduced size cell was required for X-ray CT setup for placing X-ray source as close as possible to the specimen yielding smaller voxel size and better resolution. FEI Scios Dualbeam (ThermoFisher Scientific) was used for cross-sectional images. The sample transferred was performed using air-tight transfer arm from Ar-filled glovebox to FEI Scios Dualbeam chamber for no air exposure during the transfer process. After the sample mount, liquid nitrogen and the heat exchanger was set to perform cryogenic ion beam milling and electron beam imaging to minimize the Li damage. The ion-beam milling to prepare the cross-section of samples were performed using Ga^+ source. The sample was milled at 30 kV and 65 nA, and cleaned at 30 nA and 15 nA afterwards. All the electron beam imaging was done using 5 kV and 0.1 nA settings.

2.3. Electrochemical Characterization

Two titanium rods were used as current collectors at each end of the Li metal. The solid-state cell was fabricated by first putting 75 mg of LPSCl in a 10 mm inner diameter polyether ether ketone holder, which was then compressed between two titanium rods at 370 MPa. For Li metal symmetric cells, punched Li metal was inserted on top and bottom of as-fabricated LPSCl pellet. After enclosing solid state cell of Li-SSE-Li using titanium rods, the cell was pressed at 25 MPa to facilitate better contact between the Li metal and SSE interface for 1 min. to 24 hr. The cells

were released to 5 MPa before cycling starts. For a constant pressure setup, blue dye springs (McMaster-Carr, 1804N16) were placed between top plate and nuts for all three screws. Springs were selected based on two criteria: (i) Maximum load of spring (53 lb) should be larger than load from cell cycling pressure. The cell load was calculated based on 5 MPa for the area of 0.785 cm^2 cell. The calculated load was divided by three since the load is divided by three springs, yielding 29.4 lb of load for each spring (ii) Spring rate should be high enough not need to be compressed too much to achieve certain pressure. With the spring rate of 5.5 lb/mm in this work, 5.35 mm compression is needed to achieve 5 MPa. The full cell configuration follows the same protocol except one Li side is replaced with cathode composite. Cathode composite loadings for full cell ranged from 6.4 mg/cm^2 to 51.0 mg/cm^2. All cell cycling were performed at 40°C using the compact muffle furnace (MTI KSL-1100X) in the Argon-filled atmosphere glovebox. The battery cells were cycled using a Neware Battery cycler and analyzed with BTS900 software. During the cycling, in-situ home-made load reader was used to get the pressure reading every 10 sec. For the EIS cell, the 13 mm diameter plunger (area of 1.33 cm^2) was used to fabricate Li | LPSCl | Li cell. 300 mg of LPSCl was compressed at 370 MPa to make the pellet and Li chip was inserted on both end of the pellet. EIS measurements were conducted using Solartron 1260 impedance analyzer for Li | LPSCl | Li symmetric cell every 20 minutes after setting the cell stack pressure to 25 MPa. The frequency range was from 10 MHz to 0.1 Hz, with an applied AC potential of 10 mV. Direct current polarization was conducted to measure the electronic conductivity of LPSCl by applying the voltage of 100 mV for 3 min.

3. Results and Discussion

3.1 The critical current densities of Li metal symmetric cells

The current fabrication process for the Li metal cell, schematized in Figure 1a, consists of three steps: 1) densifying the LPSCl pellet at 370 MPa, 2) adding Li metal foils on both ends of the cell and 3) pressing at 25 MPa briefly to ensure good Li metal/SSE contact. Lastly, the pressure is then released to 5 MPa for the cell cycling. These protocols were described in our previous work [38] and the *operando* pressure monitoring was conducted with our custom-built pressure recording system (Figure S2). While the amount of compaction pressure used to fabricate ASSBs is routinely reported, the amount of time pressure applied when the Li metal anode is added and thus, the degree of Li metal deformation and uniformity has never been reported in the previous reports. The degree of Li metal deformation will affect the degree of contact and uniformity at the Li metal/SSE interface. To verify the validity of our pressure control setup, the stack pressures of the Li symmetric cell were monitored during both the initial contact at 25 MPa and the subsequent plating/stripping cycling at 5 MPa. Figure 1b shows that the pressure drop during the initial contact was severe, where stack pressures dropped from 25 MPa applied initially to 21.1 MPa after 24 hours. Subsequently, the cell was released to 5 MPa and started plating/stripping, during which little to no change was observed (Figure 1b, yellow shaded). The cycling data after setting to 5 MPa will be discussed later. To rule out any effects of different thermal expansion coefficients from various cell components, the stack pressures of an empty cell and the standard symmetric cell were monitored and compared (Figure 1c, d). From the pressure trends (24-hour monitoring at room temperature and 40°C), both cells showed a rapid pressure drop during the first 30 minutes, losing 2.2 MPa (room temperature) and 5.6 MPa (40°C) during the initial 30 minutes, followed by a gradual decrease in pressure after one hour. The amount of pressure drop after 24 hours is smaller at room temperature (Figure 1c) compared to at 40°C (Figure 1d), which indicates a larger amount of Li deformation under elevated temperature

conditions. This is consistent with the lower yield strength of Li at higher temperatures [40], which facilitates deformation and is consistent with our observations. The Li symmetric cell pressure trend highlights two important points: i) When 25 MPa of stack pressure is applied during cell fabrication, Li metal deformation occurs, and saturation of the deformation is observed after 10 hours. ii) The pressure during the plating/stripping of the Li metal symmetric cell remains unchanged at all times.

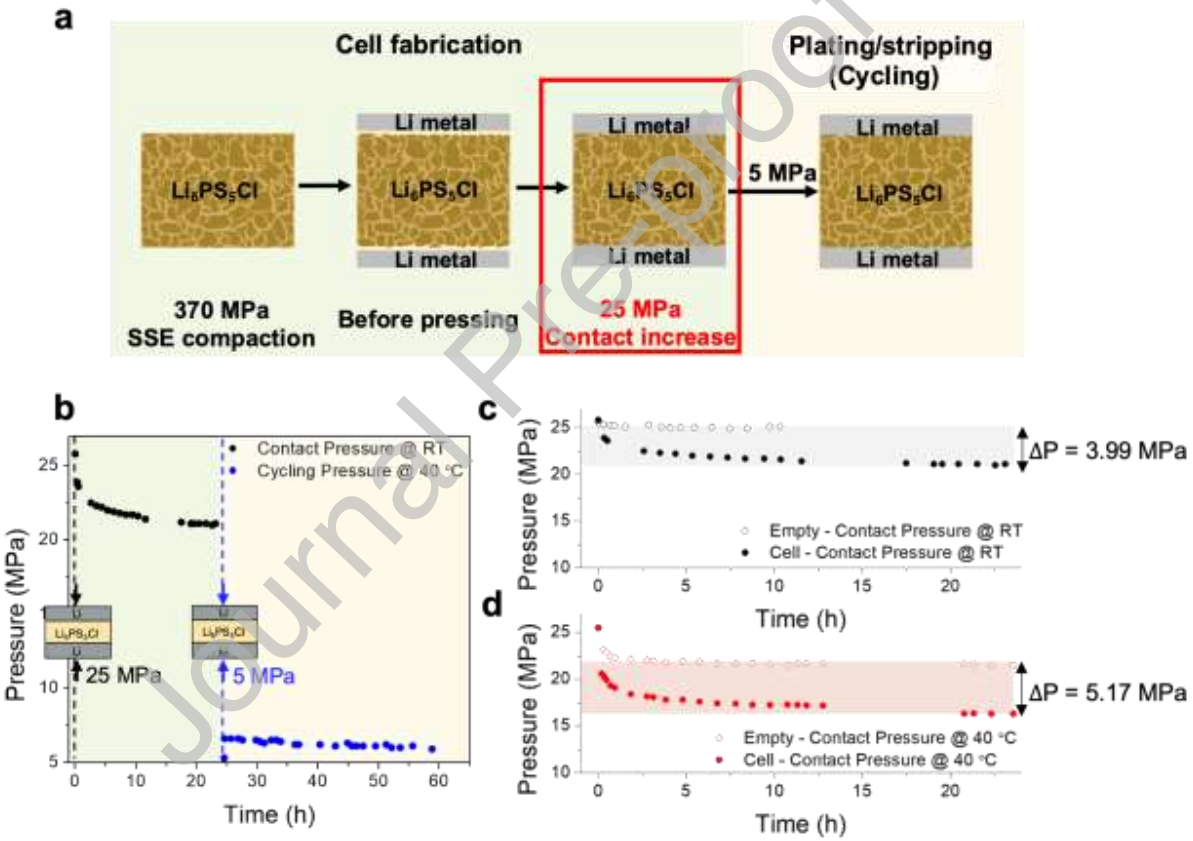

Figure 1. a) Schematic showing the fabrication protocol of Li metal symmetric cell, where 25 MPa is applied to improve the Li metal/SSE contact interface. b) Pressure monitoring during contact hold after applying 25 MPa at room temperature for 24 hours (green) and

plating/stripping at 5 MPa and 40°C (yellow). Pressure monitoring of empty plunger cell and Li metal symmetric cell after applying 25 MPa at c) room temperature and d) 40°C for 24 hours.

Following pressure monitoring during contact hold time, ramp tests (a stepwise increase of the constant current plating/stripping of lithium) of the symmetric cells were conducted (Figure 2a). This experiment allows us to evaluate the CCD of Li metal in a Li | LPSCl | Li symmetric cell and compare it to the literature. However, as seen in Figure 2a, we noticed that depending on the contact hold time, the CCD of the cells showed inconsistent values, such as 0.88 mA/cm^2 when pressure was applied for 1 min, and 2.15 mA/cm^2 after a 30 min contact hold. Figure 2b shows the CCD trend as a function of the 25 MPa contact hold time. It was found that the CCD increased as the hold time was increased up to 30 min, the CCD increased, but it decreased when it held longer than 30 min. The CCD range in our experiment (0.3 – 2.15 mA/cm^2) agrees with the wide range of CCDs reported in the literature [8-22, 38, 39, 40]. The CCD increase over the first 30 mins can be attributed to improved contact between the Li metal and SSE, leading to a lower effective current density due to the higher area of contact and more uniform current flow distribution. From the onset at 25 MPa, the pressure dropped to 23 MPa within 30 min (Figure 1b), indicating that any voids at the interface between Li metal and the SSE were filled with deformed Li metal. Impedance measurements were also conducted during this period, showing an initial rapid drop in impedance during the first 20 min and slowly decaying afterward (Figure S3). After the 1-min holding cell was shorted at 0.88 mA/cm^2, the X-ray computed tomography (CT) was used to observe the Li/SSE interface and 3-dimensional morphology of the solid-state cell (Figure 2c, Figure S4). Disparities in image contrast were used to assign the white regions and gray areas in the 3D reconstructed image to Li metal and SSE,

respectively. Evidence of Li dendrite growth was observed within the SSE layer originating from the Li metal. The voltage response after cell shorting was caused by the Li dendrite growth and its penetration through the SSE layer. When the contact time is longer than 30 min, CCDs are reduced again as shown in the red region in Figure 2b. This could be attributed to the excessive creep behavior of Li metal inside the SSE pellet which results in the more favorable short-circuit at a lower CCD [38]. Please note that the electronic conductivity of LPSCl used in our study was 1.8×10^{-8} S/cm (Figure S5), lower than LLZO and Li_3PS_4, and thus, there is a low chance of forming Li dendrite from the electronic pathway of electrolyte layer due to the lower electronic conductivity of LPSCl.

By increasing the holding time, the effective contact area between Li metal and the SSE will increase due to the deformation of Li metal at the interface which can improve the uniformity for local current distribution and thus CCD. The correlation between Li deformation and the measured CCD was investigated with the microscopic observation of a cross-sectional image by using a cryogenic focused ion beam (cryo-FIB) after pressing the Li metal anode on the SSE pellet. Since ion beam milling at room temperature can damage Li metal which results in both an altered morphology and chemistry [44], cryo-FIB was used to obtain intact Li metal interface images. Figure 2d shows the cross-sectional scanning electron microscope (SEM) images for 25 MPa pressured Li/SSE interface after contact-holding a 1 min and a 30 min. These cells were not cycled to investigate interfacial contact as a function of contact hold time. For the 30-min holding sample, the interface between the Li and SSE has no pores and the Li is fully in contact with the SSE, while the 1-min holding sample shows numerous voids at the interface, indicating poor Li contact with the SSE. The result of having better contact for longer contact hold time is expected based on previous studies investigating Li metal deformation near room

temperature. The mechanical deformation test showed Li metal can substantially fill the voids, even at pressures less than 5 MPa measured by Ding *et al* [45]. Moreover, Zhang *et al.* demonstrated that Li-SSE contact area increased over time under 1.5 – 7.5 MPa of stack pressure [46]. This study implied that the contact area of Li and SSE could increase over time through mechanical deformation of Li. The fraction in contact increased with time, showing the Li deformation-induced contact increase was rapid for the first 30 min and slowly decayed after that, which corresponds well with our pressure reduction due to Li deformation in Figure 2b, d. Thus, considering the soft mechanical properties of Li and its time-dependent deformation, the Li metal contact time under applied pressure is a vital parameter to report.

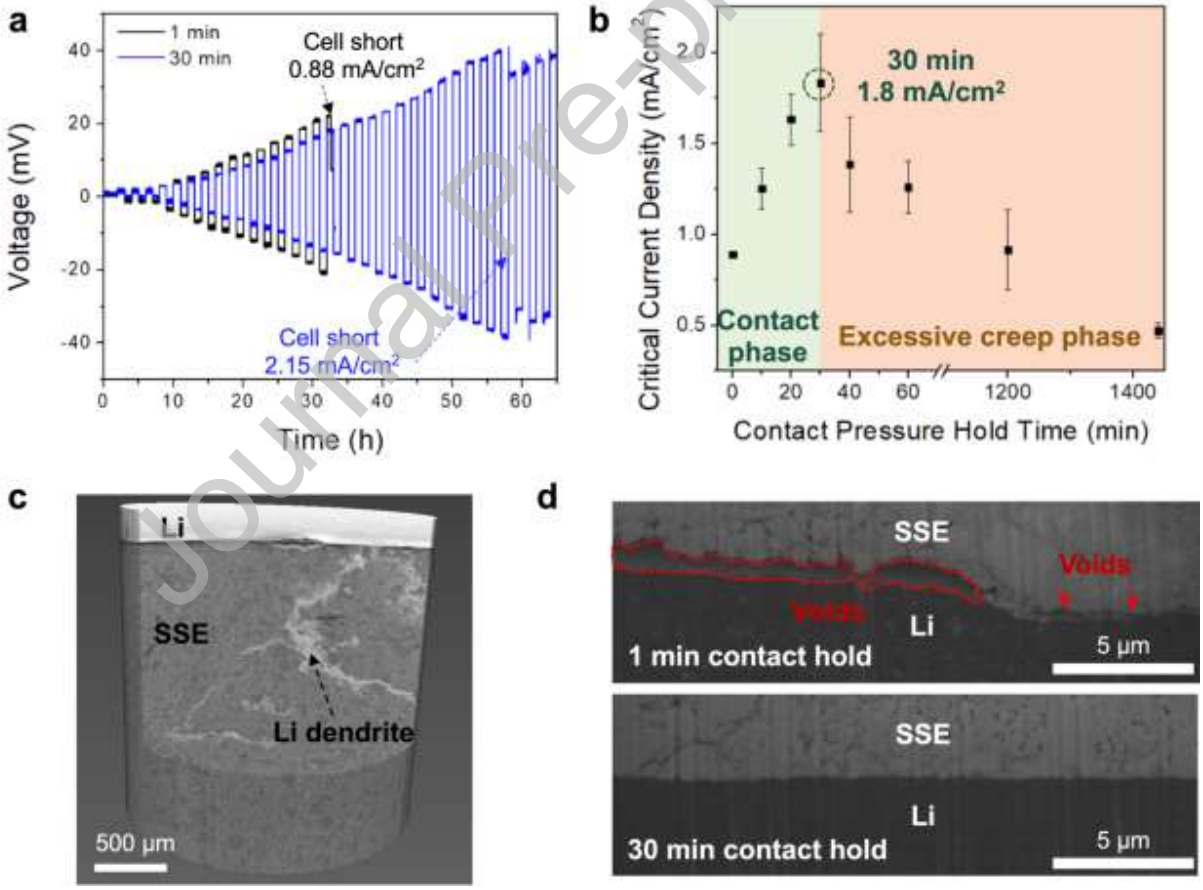

Figure 2. a) Critical current density (CCD) ramping test of Li symmetric cells, where a contact pressure of 25 MPa was applied for 1 min (black) and 30 min (blue). b) The CCD trend as a function of the contact hold time at 25 MPa. c) X-ray computed tomography of one end of the Li metal symmetric cell after shorting. d) Cross-sectional SEM images of Li/SSE interface contacted at 25 MPa for 1 min and 30 min. The electron imaging and FIB milling were conducted in cryogenic conditions to minimize damage to the Li metal.

3.2 The critical current density of Li metal full cells

As previously mentioned, reports using Li metal full cells appear to display a lower CCD compared to Li metal symmetric cells. Most literature reports attribute low CCDs to the intrinsic interfacial instability between Li metal and various SSEs, or high impedance growth at the Li metal – SSE interface [8]. However, these explanations do not agree with the symmetric vs full cell trends observed. As the same Li metal – SSE interface is utilized in both the symmetric and full cells, it indicates that the contrasting CCDs reported in both cell configurations are not correlated with the Li metal – SSE's interfacial properties, but rather a cell level phenomenon induced by the fact that a cathode is used in the full cell and not in a symmetric cell. Given the understanding that Li metal undergoes a significant volume change during plating and stripping (1 mAh/cm^2 ≈ 5 μm) [47], overall cell volume change in full cells is expected to be substantial compared to symmetric cells where negligible net volume change is expected, regardless of areal capacity exchanged. Thus, unlike in symmetric cells, it is necessary to consider both cathode and anode expansion/shrinkage in full cells, because volume changes during cycling can induce significant changes in cell stack pressure, and in turn, affect its CCD.

As a thought experiment, the volume change scenario for a symmetric cell and a full cell model is illustrated in Figure 3a**.** The pressure does not change during symmetric cell cycling theoretically, because stripped Li from one side would be plated on the counter electrode. However, in a full cell, Li metal will grow in thickness while the cathode shrinkage is significantly smaller when the cell is charged, leading to an overall volume expansion of the whole cell (Table S1). During discharge, almost all the Li will be sent back to the cathode, and the volume will once again shrink. Therefore, pressure increase/decrease apparent during charge and discharge is mainly due to the volume change of the Li metal anode. As the volume change largely comes from Li metal plating, a higher degree of pressure change is expected when the cell capacity is increased, resulting in conditions deviating further away from that of a symmetric cell.

To probe the CCDs of full cells, NCM811 | LPSCl | Li cells with different cathode loadings were cycled using the stepwise current ramping protocol (Figure 3b). Please note that the optimum fabrication protocol of Li metal anode which is the 30-min contact at 25 MPa followed by release to 5 MPa was used for an anode preparation. With higher cathode loadings, pressure changes during charge/discharge were more severe because the amount of plated Li on the anode during charging is larger. Therefore, the stack pressure change during cycling has a linear correlation with the cathode loading (Figure 3c). In particular, with a cathode loading of 6.4 mg/cm^2, the absolute pressure change is 0.73 MPa whereas the absolute pressure change reaches 2.14 MPa for loading of 25.5 mg/cm^2 and 6.2 MPa for loading of 51.0 mg/cm^2. The CCDs obtained from full cells were in the range of 0.3 – 1.0 mA/cm^2, showing a decreasing trend with higher cathode loading. The low CCD for higher loading cells could be attributed to higher cell pressure from thicker Li plating. There are three major Li^+ migrations and Li fluxes

involved during plating/stripping of lithium: i) Li^+ migration from applied current during cycling ($J_{Li^+ migration}$), ii) Self-diffusion of Li atoms from concentration gradient ($J_{Li\ diffusion}$), 3. Li creep deformation from the stack pressure ($J_{Li\ creep}$) [37]. If these three fluxes maintain the balance, ($J_{Li^+ migration} = J_{Li\ diffusion} + J_{Li\ creep}$), the dendritic growth of Li could be inhibited [48]. For the Figure 3d case, cells with the same initial stack pressure but with various cathode loadings, the $J_{Li^+ migration}$ would be similar for all cells at the same current densities. However, the higher cathode loading cells would eventually operate at higher pressure due to the thicker Li plating on the anode side. This higher operating pressure would yield a larger flux of Li ($J_{Li\ creep}$) to the interface, which results in the imbalance of the fluxes and shorts the cells.

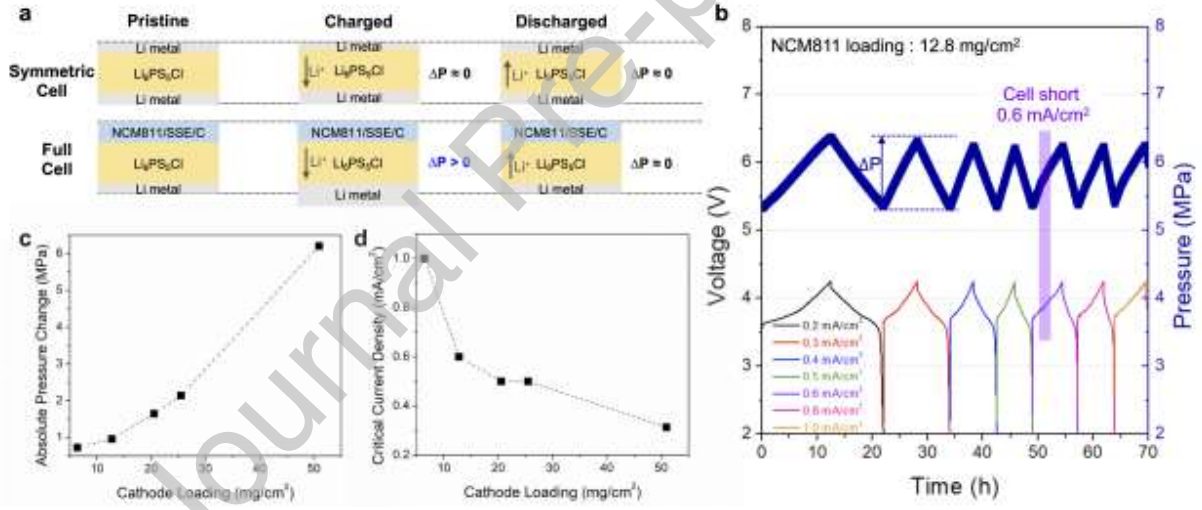

Figure 3. a) Schematic of the pressure change during cycling in a Li metal symmetric cell and a full cell. b) The *operando* pressure monitoring and voltage curve during cycling of Li metal full cells. All cells were cycled with the stepwise constant current; 0.2 to 1.0 mA/cm^2. c) Absolute pressure changes during cycling and d) Critical current densities of Li metal full cells as a function of cathode loading. The absolute pressure change was calculated by subtracting the first

cycle minimum pressure from the first cycle maximum pressure. All of the cyclings were performed at an initial stack pressure of 5 MPa and 40°C.

3.3 The operating pressure control of Li metal full cells

Given that the cathode loading presents a direct impact on the degree of pressure change and the resulting CCD, operating the cells at a constant pressure could create conditions more similar to symmetric cells and allow for higher CCDs in full cells. Therefore, the cell setup was modified to incorporate springs that can compensate for the volume expansion and shrinkage of the cell. This constant pressure setup, therefore, allows us to cycle the full cell at nearly constant pressure. The springs were selected based on their maximum load (which should be higher than the load applied during cycling) and their spring constants, to ensure that we can reach the target pressure with a reasonable compression of the springs.

The CCDs for Li-ASSB cells using setups with no springs (the fixed gap, Figure 4a) and with springs (the constant pressure, Figure 4b) in the cell holder were examined using similar ramping tests. In the fixed-gap cell, severe pressure change was observed during the charge and discharge process, around 140% pressure increase (6.96 MPa after 1st cycle charge) at the end of charge, exhibiting shorted behavior during the charging at a current density of 0.5 mA/cm^2 (Figure 4c, e). However, in the cell with springs, the pressure deviation was only 104% (5.21 MPa after 1st cycle charge) which is much less severe than fixed-gap cell and more stable during charging and discharging as expected, allowing the cell to cycle at a much higher current density until shorting at 1.0 mA/cm^2 (Figure 4d, f). The creep deformation rate of Li metal increases as the external compressive pressure gets higher [45]. The Li creep rate at 30°C was 0.06 μm/h at 2.2 MPa and 0.42 μm/h at 3.5 MPa. From this data, we could see only 1.2 MPa difference in

stack pressure would result in 7 times higher creep rate of lithium. Therefore, by changing fixed gap setup to constant pressure setup, the Li would not have such high Li creep rate within the full cell. The long-term cycling performance of the fixed gap and constant pressure setup was examined in Figure S6. With the same loading and the cycling protocol of 0.5 mA/cm^2 long cycling after the formation cycles, the fixed gap setup cell shorted at 2nd cycle, whereas the constant pressure cell operated more than 50 cycles without shorting. As such, the CCD of the Li metal full cell can be improved by enabling the constant pressure cycling, which gives us the methodologic clue to solve the volume change deriven pressure accumulation in the practical Li metal full cell.

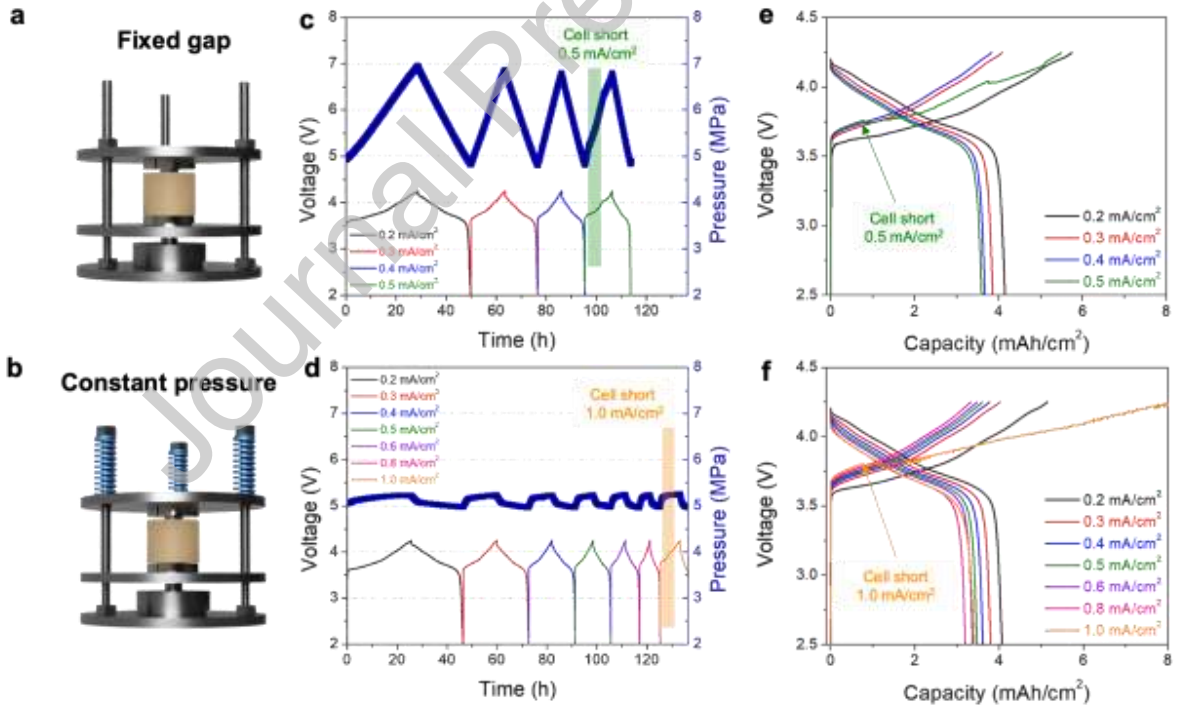

Figure 4. The schematic of the cell cycling setups for a) fixed gap and b) constant pressure. The NCM811 loading of both cells were 25.5 mg/cm^2. The *operando* pressure monitoring and

corresponding voltage profiles of NCM811 | LPSCl | Li metal cells with c, e) fixed gap and d, f) constant pressure setup at ramping current densities. All the cycling was performed at an initial stack pressure of 5 MPa at 40°C.

To probe the effects of constant pressure at lower pressures, fixed gap and constant pressure cells were tested at 1 MPa, 3 MPa, and 5 MPa (Figure 5). At 1 MPa, both constant gap and constant pressure cells showed the same low CCD of 0.3 mA/cm^2, whereas constant pressure cell exhibited slightly higher CCD of 0.6 mA/cm^2 than constant gap cell of 0.4 mA/cm^2 at 3 MPa. Constant pressure effect dominates more from 5 MPa, where the CCD difference of constant pressure and fixed gap is 0.6 mA/cm^2. This trend is not surprising based on the Li creep behavior observed in Figure 1 and 2. At 1 MPa, the stack pressure applied is insufficient to provide a creep deformation rate high enough to ensure good interfacial contact between the Li metal and the SSE. This results in non-uniform Li plating and results in early cell failure regardless of the effects of constant pressure. While a higher creep deformation rate at 3 MPa allows the effects of constant pressure applied to be detected, previous reports have also found void accumulation at the interface at 3 MPa [37], indicating that 3 MPa is still insufficient to maintain good contact. At 5 MPa, sufficient Li creep was achieved and thus able to effectively double the CCD detected when constant pressure is applied. This pressure value agrees with the literature reported values for ideal Li ASSB full cells [4]. While higher stack pressures may produce greater effects on CCD, stack pressures of 10 MPa or greater have been found to induce excessive Li creep into and through the SSE separator, also inducing cell failure [38]. The results in this work, along with findings in the literature suggests that Li ASSBs are best operated within a narrow range of

stack pressures, highlighting the need for constant pressure operation to maximize CCD in Li ASSBs.

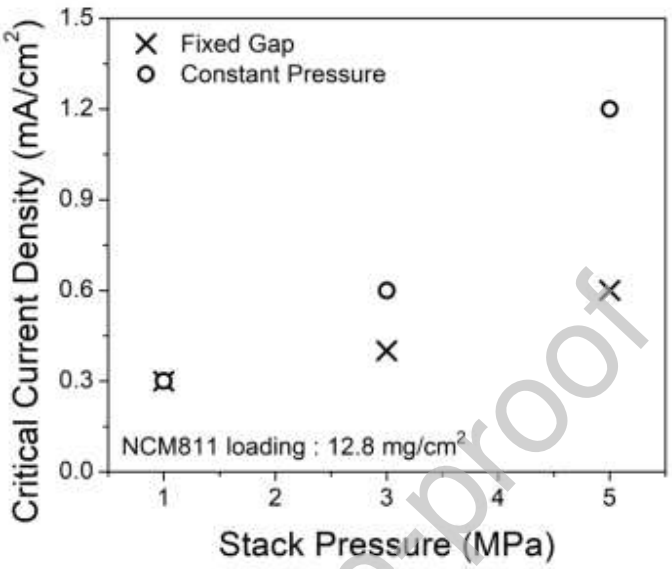

Figure 5. The CCD trends of fixed gap (cross symbol) and constant pressure (circle symbol) cells with the initial stack pressure of 1, 3, and 5 MPa. The NCM811 loading of all cells were 12.8 mg/cm^2.

4. Conclusions

The previously reported CCDs of Li-ASSBs exhibited extensive variations, with evident disparities between Li metal symmetric cells and Li metal full cells. In this study, we investigated critical fabrication parameters that can resolve the discrepancies the in reported CCDs. In particular, the contact hold time during cell assembly is a crucial consideration, which affects the formation of solid physical contact between Li metal and SSE. During this hold time, Li metal undergoes time dependent mechanical deformation that can alter the effective contact area. By improving the interfacial contact and uniformity, the CCD can thus be improved and

achieved more reproducibly. In addition, we have confirmed the mismatch in terms of CCDs and corresponding performance between symmetric and full cell, where contributions from the cathode must be considered. The volume change in Li metal full cells is inevitable due to expansion and contraction of electrodes from Li metal plating and stripping at anode during cell cycling which cannot compensate from the cathode side. The continuous volume change driven stress accumulation within the confined cell was examined via the *operando* pressure monitoring during cell cycling. The increased stack pressure resulted in the premature shorting of the full cell and the trend was correlated to the cathode loading, which showed that cells with higher cathode loading exhibited much more severe pressure change, subsequently shorting at lower current densities. We have identified anode volume change, which accumulates to net stack pressure change, as an important cause of cell shorting and have designed a constant pressure cell architecture which utilizes springs to mitigate pressure changes during cycling. This improved setup demonstrates the necessity of maintaining constant stack pressure during cycling and has enabled higher current density operation for Li-ASSBs, specifically near room temperature.

Acknowledgements

This work was supported by LG Energy Solution – UC San Diego Frontier Research Laboratory via the Open Innovation program. This work was performed in part at the San Diego Nanotechnology Infrastructure (SDNI) of UCSD, a member of the National Nanotechnology Coordinated Infrastructure, which is supported by the National Science Foundation (Grant ECCS-2025752)

CRediT Authorship Contribution Statement

So-Yeon Ham: Conceptualization, Data curation, Methodology, Formal analysis, Investigation, Writing − original draft, Visualization. **Hedi Yang**: Investigation, Validation. **Omar Nunez-cuacuas**: Methodology, Formal analysis. **Darren H. S. Tan**: Investigation, Methodology, Conceptualization. **Yu-Ting Chen**: Investigation, Validation. **Grayson Deysher**: Formal analysis, Validation. **Ashley Cronk**: Investigation, Visualization. **Philip Ridley**: Methodology. **Jean-Marie Doux**: Methodology, Formal analysis, Supervision. **Erik A. Wu:** Methodology, Formal analysis. **Jihyun Jang**: Conceptualization, Formal analysis, Data curation, Writing – review & editing, Supervision. **Ying Shirley Meng**: Formal analysis. Software, Writing – review & editing, Supervision, Project administration, Funding acquisition.

Declaration of interests

☒The authors declare that they have no known competing financial interests or personal relationships that could have appeared to influence the work reported in this paper.

☐The authors declare the following financial interests/personal relationships which may be considered as potential competing interests:

References

[1] K.N. Wood, M. Noked, N.P. Dasgupta, Lithium metal anodes: Toward an improved understanding of coupled morphological, electrochemical, and mechanical behavior, ACS Energy Letters. 2 (2017) 664–672. https://doi.org/10.1021/acsenergylett.6b00650.

[2] K.B. Hatzell, X.C. Chen, C.L. Cobb, N.P. Dasgupta, M.B. Dixit, L.E. Marbella, M.T. McDowell, P.P. Mukherjee, A. Verma, V. Viswanathan, A.S. Westover, W.G. Zeier, Challenges in Lithium Metal Anodes for Solid-State Batteries, ACS Energy Lett. 5 (2020) 922–934. https://doi.org/10.1021/acsenergylett.9b02668.

[3] C. Wang, J. Liang, Y. Zhao, M. Zheng, X. Li, X. Sun, All-solid-state lithium batteries enabled by sulfide electrolytes: From fundamental research to practical engineering design, Energy and Environmental Science. 14 (2021) 2577–2619. https://doi.org/10.1039/d1ee00551k.
[4] Y.G. Lee, S. Fujiki, C. Jung, N. Suzuki, N. Yashiro, R. Omoda, D.S. Ko, T. Shiratsuchi, T. Sugimoto, S. Ryu, J.H. Ku, T. Watanabe, Y. Park, Y. Aihara, D. Im, I.T. Han, High-energy long-cycling all-solid-state lithium metal batteries enabled by silver–carbon composite anodes, Nature Energy. 5 (2020) 299–308. https://doi.org/10.1038/s41560-020-0575-z.
[5] T. Dussart, N. Rividi, M. Fialin, G. Toussaint, P. Stevens, C. Laberty-Robert, Critical Current Density Limitation of LLZO Solid Electrolyte: Microstructure vs Interface, J. Electrochem. Soc. 168 (2021) 120550. https://doi.org/10.1149/1945-7111/ac44be.
[6] F. Shen, M.B. Dixit, X. Xiao, K.B. Hatzell, Effect of Pore Connectivity on Li Dendrite Propagation within LLZO Electrolytes Observed with Synchrotron X-ray Tomography, ACS Energy Lett. 3 (2018) 1056–1061. https://doi.org/10.1021/acsenergylett.8b00249.
[7] T. Krauskopf, B. Mogwitz, C. Rosenbach, W.G. Zeier, J. Janek, Diffusion Limitation of Lithium Metal and Li–Mg Alloy Anodes on LLZO Type Solid Electrolytes as a Function of Temperature and Pressure, Adv. Energy Mater. 9 (2019) 1902568. https://doi.org/10.1002/aenm.201902568.
[8] A. Sharafi, H.M. Meyer, J. Nanda, J. Wolfenstine, J. Sakamoto, Characterizing the Li–Li7La3Zr2O12 interface stability and kinetics as a function of temperature and current density, Journal of Power Sources. 302 (2016) 135–139. https://doi.org/10.1016/j.jpowsour.2015.10.053.
[9] Z. Xu, H. Zhang, T. Yang, X. Chu, Y. Xie, Q. Wang, Y. Xia, W. Yang, Physicochemically dendrite-suppressed three-dimensional fluoridation solid-state electrolyte for high-rate lithium metal battery, Cell Reports Physical Science. 2 (2021) 100644. https://doi.org/10.1016/j.xcrp.2021.100644.
[10] W. Chang, R. May, M. Wang, G. Thorsteinsson, J. Sakamoto, L. Marbella, D. Steingart, Evolving contact mechanics and microstructure formation dynamics of the lithium metal-Li7La3Zr2O12 interface, Nat Commun. 12 (2021) 6369. https://doi.org/10.1038/s41467-021-26632-x.
[11] J. Wang, Z. Zhang, H. Ying, S. Zhang, H. Tan, G. Han, W.-Q. Han, An effective artificial layer boosting high-performance all-solid-state lithium batteries with high coulombic efficiency, Journal of Materiomics. (2021) S2352847821001490. https://doi.org/10.1016/j.jmat.2021.10.006.
[12] S. Palakkathodi Kammampata, H. Yamada, T. Ito, R. Paul, V. Thangadurai, The activation entropy for ionic conduction and critical current density for Li charge transfer in novel garnet-type $Li_{6.5}La_{2.9}A_{0.1}Zr_{1.4}Ta_{0.6}O_{12}$ (A = Ca, Sr, Ba) solid electrolytes, J. Mater. Chem. A. 8 (2020) 2581–2590. https://doi.org/10.1039/C9TA12193E.
[13] M. Wang, J.B. Wolfenstine, J. Sakamoto, Temperature dependent flux balance of the Li/Li7La3Zr2O12 interface, Electrochimica Acta. 296 (2019) 842–847. https://doi.org/10.1016/j.electacta.2018.11.034.
[14] L. Cheng, W. Chen, M. Kunz, K. Persson, N. Tamura, G. Chen, M. Doeff, Effect of Surface Microstructure on Electrochemical Performance of Garnet Solid Electrolytes, ACS Appl. Mater. Interfaces. 7 (2015) 2073–2081. https://doi.org/10.1021/am508111r.
[15] R. Hongahally Basappa, T. Ito, T. Morimura, R. Bekarevich, K. Mitsuishi, H. Yamada, Grain boundary modification to suppress lithium penetration through garnet-type solid

electrolyte, Journal of Power Sources. 363 (2017) 145–152. https://doi.org/10.1016/j.jpowsour.2017.07.088.
[16] Y. Huang, B. Chen, J. Duan, F. Yang, T. Wang, Z. Wang, W. Yang, C. Hu, W. Luo, Y. Huang, Graphitic Carbon Nitride (g-C_3N_4): An Interface Enabler for Solid-State Lithium Metal Batteries, Angew. Chem. Int. Ed. 59 (2020) 3699–3704. https://doi.org/10.1002/anie.201914417.
[17] K. (Kelvin) Fu, Y. Gong, B. Liu, Y. Zhu, S. Xu, Y. Yao, W. Luo, C. Wang, S.D. Lacey, J. Dai, Y. Chen, Y. Mo, E. Wachsman, L. Hu, Toward garnet electrolyte–based Li metal batteries: An ultrathin, highly effective, artificial solid-state electrolyte/metallic Li interface, Sci. Adv. 3 (2017) e1601659. https://doi.org/10.1126/sciadv.1601659.
[18] C. Wang, Y. Gong, J. Dai, L. Zhang, H. Xie, G. Pastel, B. Liu, E. Wachsman, H. Wang, L. Hu, In Situ Neutron Depth Profiling of Lithium Metal–Garnet Interfaces for Solid State Batteries, J. Am. Chem. Soc. 139 (2017) 14257–14264. https://doi.org/10.1021/jacs.7b07904.
[19] T. Deng, X. Ji, Y. Zhao, L. Cao, S. Li, S. Hwang, C. Luo, P. Wang, H. Jia, X. Fan, X. Lu, D. Su, X. Sun, C. Wang, J. Zhang, Tuning the Anode–Electrolyte Interface Chemistry for Garnet-Based Solid-State Li Metal Batteries, Adv. Mater. 32 (2020) 2000030. https://doi.org/10.1002/adma.202000030.
[20] S. Xiong, Y. Liu, P. Jankowski, Q. Liu, F. Nitze, K. Xie, J. Song, A. Matic, Design of a Multifunctional Interlayer for NASCION-Based Solid-State Li Metal Batteries, Adv. Funct. Mater. 30 (2020) 2001444. https://doi.org/10.1002/adfm.202001444.
[21] X. Ji, S. Hou, P. Wang, X. He, N. Piao, J. Chen, X. Fan, C. Wang, Solid-State Electrolyte Design for Lithium Dendrite Suppression, Adv. Mater. 32 (2020) 2002741. https://doi.org/10.1002/adma.202002741.
[22] H. Huo, J. Liang, N. Zhao, X. Li, X. Lin, Y. Zhao, K. Adair, R. Li, X. Guo, X. Sun, Dynamics of the Garnet/Li Interface for Dendrite-Free Solid-State Batteries, ACS Energy Lett. 5 (2020) 2156–2164. https://doi.org/10.1021/acsenergylett.0c00789.
[23] X. Yao, D. Liu, C. Wang, P. Long, G. Peng, Y.-S. Hu, H. Li, L. Chen, X. Xu, High-Energy All-Solid-State Lithium Batteries with Ultralong Cycle Life, Nano Lett. 16 (2016) 7148–7154. https://doi.org/10.1021/acs.nanolett.6b03448.
[24] M.A. Kraft, S. Ohno, T. Zinkevich, R. Koerver, S.P. Culver, T. Fuchs, A. Senyshyn, S. Indris, B.J. Morgan, W.G. Zeier, Inducing High Ionic Conductivity in the Lithium Superionic Argyrodites $Li_{6+x}P_{1-x}Ge_xS_5I$ for All-Solid-State Batteries, J. Am. Chem. Soc. 140 (2018) 16330–16339. https://doi.org/10.1021/jacs.8b10282.
[25] W. Zhang, D.A. Weber, H. Weigand, T. Arlt, I. Manke, D. Schröder, R. Koerver, T. Leichtweiss, P. Hartmann, W.G. Zeier, J. Janek, Interfacial Processes and Influence of Composite Cathode Microstructure Controlling the Performance of All-Solid-State Lithium Batteries, ACS Appl. Mater. Interfaces. 9 (2017) 17835–17845. https://doi.org/10.1021/acsami.7b01137.
[26] G.T. Hitz, D.W. McOwen, L. Zhang, Z. Ma, Z. Fu, Y. Wen, Y. Gong, J. Dai, T.R. Hamann, L. Hu, E.D. Wachsman, High-rate lithium cycling in a scalable trilayer Li-garnet-electrolyte architecture, Materials Today. 22 (2019) 50–57. https://doi.org/10.1016/j.mattod.2018.04.004.
[27] J. Peng, D. Wu, F. Song, S. Wang, Q. Niu, J. Xu, P. Lu, H. Li, L. Chen, F. Wu, High Current Density and Long Cycle Life Enabled by Sulfide Solid Electrolyte and Dendrite-

Free Liquid Lithium Anode, Adv Funct Materials. 32 (2022) 2105776. https://doi.org/10.1002/adfm.202105776.
[28] Y. Su, L. Ye, W. Fitzhugh, Y. Wang, E. Gil-González, I. Kim, X. Li, A more stable lithium anode by mechanical constriction for solid state batteries, Energy Environ. Sci. 13 (2020) 908–916. https://doi.org/10.1039/C9EE04007B.
[29] L. Ye, X. Li, A dynamic stability design strategy for lithium metal solid state batteries, Nature. 593 (2021) 218–222. https://doi.org/10.1038/s41586-021-03486-3.
[30] D.H.S. Tan, Y.-T. Chen, H. Yang, W. Bao, B. Sreenarayanan, J.-M. Doux, W. Li, B. Lu, S.-Y. Ham, B. Sayahpour, J. Scharf, E.A. Wu, G. Deysher, H.E. Han, H.J. Hah, H. Jeong, J.B. Lee, Z. Chen, Y.S. Meng, Carbon-free high-loading silicon anodes enabled by sulfide solid electrolytes, Science. 373 (2021) 1494–1499. https://doi.org/10.1126/science.abg7217.
[31] Y. Lu, C. Zhao, H. Yuan, X. Cheng, J. Huang, Q. Zhang, Critical Current Density in Solid-State Lithium Metal Batteries: Mechanism, Influences, and Strategies, Adv. Funct. Mater. 31 (2021) 2009925. https://doi.org/10.1002/adfm.202009925.
[32] J.A. Lewis, C. Lee, Y. Liu, S.Y. Han, D. Prakash, E.J. Klein, H.-W. Lee, M.T. McDowell, Role of Areal Capacity in Determining Short Circuiting of Sulfide-Based Solid-State Batteries, ACS Appl. Mater. Interfaces. 14 (2022) 4051–4060. https://doi.org/10.1021/acsami.1c20139.
[33] Y. Chen, W. Li, C. Sun, J. Jin, Q. Wang, X. Chen, W. Zha, Z. Wen, Sustained Release-Driven Formation of Ultrastable SEI between Li_6PS_5Cl and Lithium Anode for Sulfide-Based Solid-State Batteries, Adv. Energy Mater. 11 (2021) 2002545. https://doi.org/10.1002/aenm.202002545.
[34] Y. Chen, L. Yao, X. Chen, J. Jin, M. Wu, Q. Wang, W. Zha, Z. Wen, Double-Faced Bond Coupling to Induce an Ultrastable Lithium/Li_6PS_5Cl Interface for High-Performance All-Solid-State Batteries, ACS Appl. Mater. Interfaces. 14 (2022) 11950–11961. https://doi.org/10.1021/acsami.1c24506.
[35] F. Han, A.S. Westover, J. Yue, X. Fan, F. Wang, M. Chi, D.N. Leonard, N.J. Dudney, H. Wang, C. Wang, High electronic conductivity as the origin of lithium dendrite formation within solid electrolytes, Nat Energy. 4 (2019) 187–196. https://doi.org/10.1038/s41560-018-0312-z.
[36] M.J. Wang, R. Choudhury, J. Sakamoto, Characterizing the Li-Solid-Electrolyte Interface Dynamics as a Function of Stack Pressure and Current Density, Joule. 3 (2019) 2165–2178. https://doi.org/10.1016/j.joule.2019.06.017.
[37] J. Kasemchainan, S. Zekoll, D. Spencer Jolly, Z. Ning, G.O. Hartley, J. Marrow, P.G. Bruce, Critical stripping current leads to dendrite formation on plating in lithium anode solid electrolyte cells, Nat. Mater. 18 (2019) 1105–1111. https://doi.org/10.1038/s41563-019-0438-9.
[38] J. Doux, H. Nguyen, D.H.S. Tan, A. Banerjee, X. Wang, E.A. Wu, C. Jo, H. Yang, Y.S. Meng, Stack Pressure Considerations for Room-Temperature All-Solid-State Lithium Metal Batteries, Adv. Energy Mater. 10 (2020) 1903253. https://doi.org/10.1002/aenm.201903253.
[39] H. Yan, K. Tantratian, K. Ellwood, E.T. Harrison, M. Nichols, X. Cui, L. Chen, How Does the Creep Stress Regulate Void Formation at the Lithium-Solid Electrolyte Interface during Stripping?, Advanced Energy Materials. 12 (2022) 2102283. https://doi.org/10.1002/aenm.202102283.
[40] W.S. LePage, Y. Chen, E. Kazyak, K.-H. Chen, A.J. Sanchez, A. Poli, E.M. Arruda, M.D. Thouless, N.P. Dasgupta, Lithium Mechanics: Roles of Strain Rate and Temperature and

Implications for Lithium Metal Batteries, J. Electrochem. Soc. 166 (2019) A89–A97. https://doi.org/10.1149/2.0221902jes.
[41] B. Xu, X. Li, C. Yang, Y. Li, N.S. Grundish, P.-H. Chien, K. Dong, I. Manke, R. Fang, N. Wu, H. Xu, A. Dolocan, J.B. Goodenough, Interfacial Chemistry Enables Stable Cycling of All-Solid-State Li Metal Batteries at High Current Densities, J. Am. Chem. Soc. 143 (2021) 6542–6550. https://doi.org/10.1021/jacs.1c00752.
[42] G. Liu, W. Weng, Z. Zhang, L. Wu, J. Yang, X. Yao, Densified Li6PS5Cl Nanorods with High Ionic Conductivity and Improved Critical Current Density for All-Solid-State Lithium Batteries, Nano Letters. 20 (2020) 6660–6665. https://doi.org/10.1021/acs.nanolett.0c02489.
[43] Y. Lu, C.Z. Zhao, H. Yuan, X.B. Cheng, J.Q. Huang, Q. Zhang, Critical Current Density in Solid-State Lithium Metal Batteries: Mechanism, Influences, and Strategies, Advanced Functional Materials. (2021). https://doi.org/10.1002/adfm.202009925.
[44] J.Z. Lee, T.A. Wynn, M.A. Schroeder, J. Alvarado, X. Wang, K. Xu, Y.S. Meng, Cryogenic Focused Ion Beam Characterization of Lithium Metal Anodes, ACS Energy Letters. 4 (2019) 489–493. https://doi.org/10.1021/acsenergylett.8b02381.
[45] S. Ding, L. Fairgrieve-Park, O. Sendetskyi, M.D. Fleischauer, Compressive creep deformation of lithium foil at varied cell conditions, Journal of Power Sources. 488 (2021) 229404. https://doi.org/10.1016/j.jpowsour.2020.229404.
[46] X. Zhang, Q.J. Wang, K.L. Harrison, S.A. Roberts, S.J. Harris, Pressure-Driven Interface Evolution in Solid-State Lithium Metal Batteries, Cell Reports Physical Science. 1 (2020) 100012. https://doi.org/10.1016/j.xcrp.2019.100012.
[47] S. Chen, C. Niu, H. Lee, Q. Li, L. Yu, W. Xu, J.-G. Zhang, E.J. Dufek, M.S. Whittingham, S. Meng, J. Xiao, J. Liu, Critical Parameters for Evaluating Coin Cells and Pouch Cells of Rechargeable Li-Metal Batteries, Joule. 3 (2019) 1094–1105. https://doi.org/10.1016/j.joule.2019.02.004.
[48] A. Banerjee, X. Wang, C. Fang, E.A. Wu, Y.S. Meng, Interfaces and Interphases in All-Solid-State Batteries with Inorganic Solid Electrolytes, Chem. Rev. 120 (2020) 6878–6933. https://doi.org/10.1021/acs.chemrev.0c00101.